

Sensitivity of Displaced-Beam Scintillometer Measurements of Area-Average Heat Fluxes to Uncertainties in Topographic Heights

Matthew Gruber (matthewgruber@gi.alaska.edu) and Javier Fochesatto (foch@gi.alaska.edu)

Department of Atmospheric Science, College of Natural Sciences and Mathematics, Geophysical Institute, University of Alaska Fairbanks

Oscar Hartogensis (oscar.hartogensis@wur.nl)

Meteorology and Air Quality Group, Wageningen University, the Netherlands

Abstract. Displaced-beam scintillometer measurements of the turbulence inner-scale length l_o and refractive index structure function C_n^2 resolve area-average turbulent fluxes of heat and momentum through the Monin-Obukhov similarity equations. Sensitivity studies have been produced for the use of displaced-beam scintillometers over flat terrain. Many real field sites feature variable topography. We develop here an analysis of the sensitivity of displaced-beam scintillometer derived sensible heat fluxes to uncertainties in spatially distributed topographic measurements. Sensitivity is shown to be concentrated in areas near the center of the beam and where the underlying topography is closest to the beam height. Uncertainty may be decreased by taking precise topographic measurements in these areas.

Keywords: Displaced-beam scintillometer, Effective beam height, Scintillometer error, Scintillometer uncertainty, Turbulent fluxes

1. Introduction

Displaced-beam scintillometers are useful to make measurements of turbulent heat fluxes since their footprint is much larger than other measurement devices such as sonic anemometers. Their source measurements are the index of refraction structure parameter C_n^2 and the turbulence inner scale length l_o , which are used to infer the turbulent heat fluxes (Hill, 1988; Andreas, 1992). This inference follows from equations from the Monin-Obukhov similarity hypothesis, which is a model for turbulent fluxes of heat and momentum in the atmospheric surface layer (Sorbjan, 1989). Studying the sensitivity of the derived turbulent heat flux to the uncertainties in the source measurements is important, and several studies have been published exploring the case of measurements over flat terrain (Andreas, 1989; Moroni et al., 1990; Andreas, 1992; Solignac et al., 2009). There is debate over whether the Monin-Obukhov similarity hypothesis can be applied over variable terrain since the canonical model is for flat terrain, however many scin-

tillometer field campaigns take place over variable terrain (Hartogensis et al., 2002; Meijninger et al., 2002). The turbulent fluxes are derived through equations which extend the Monin-Obukhov equations from flat terrain to variable terrain via the application of an effective beam height (Hartogensis et al., 2003; Kleissl et al., 2008; Evans and deBruin, 2011; Geli et al., 2012). The effective beam height is calculated assuming that the Monin-Obukhov surface layer profiles in height are valid over the slowly varying terrain. The research question to be asked is, if one can safely extend the Monin-Obukhov equations from flat terrain to variable terrain, then in what manner is the error propagated from the uncertainty in topography to the derived turbulent heat flux?

Through the assumptions of the Monin-Obukhov similarity hypothesis, the sensible heat flux in the atmospheric surface layer is given by

$$H_S = -\rho c_p u_* T_*, \quad (1)$$

where H_S is the sensible heat flux, ρ is the density of air, c_p is the heat capacity, u_* is the friction velocity, and T_* is the temperature scale. Resolving u_* and T_* from C_n^2 and l_o starts at another similarity equation relating $\zeta \equiv z_{eff}/L$ to T_* and u_* :

$$\zeta = \frac{\kappa G T_* z_{eff}}{u_*^2 T}, \quad (2)$$

where z_{eff} is the effective beam height of the scintillometer beam, L is the Obukhov length, κ is the Von Kármán constant, G is the acceleration due to gravity, and T is the temperature (Hartogensis et al., 2003). In equation 2 we omit the term due to humidity seen in Andreas (1992) for simplicity as it has no effect on the results here.

When $\zeta > 0$ we are in a stable atmospheric surface layer. In the stable case we have

$$\frac{C_T^2 z_{eff}^{2/3}}{T_*^2} = a(1 + c\zeta^{2/3}) \rightarrow \pm T_* = \sqrt{\frac{C_T^2}{a}} \frac{z_{eff}^{1/3}}{\sqrt{1 + c\zeta^{2/3}}}, \quad (3)$$

$$z_{eff} = \left(\int_0^1 z(u)^{-2/3} G(u) du \right)^{-3/2}, \quad (4)$$

$$u_*^3 = \frac{\kappa z_{eff} \epsilon}{(1 + h\zeta^{3/5})^{3/2}} \rightarrow u_*^2 = \frac{\kappa^{2/3} z_{eff}^{2/3} \epsilon^{2/3}}{(1 + h\zeta^{3/5})}, \quad (5)$$

where a , c and h are empirical constants (Wyngaard et al., 1971; Wyngaard and Coté, 1971), $z(u)$ is the height profile of the beam above

the ground where u is the normalized distance along the beam, $G(u)$ is the path weighting function, C_T^2 is the temperature structure parameter which is inferred from C_n^2 , and z_{eff} is the effective beam height assuming that the C_T^2 profile satisfies equation 3 for any z along $z(u)$ (Andreas, 1992; Hartogensis et al., 2003). The turbulent dissipation rate ϵ is directly related to l_o by

$$l_o = \frac{(9\Gamma(1/3)KD(\rho, T))^{3/4}}{\epsilon^{1/4}}, \quad (6)$$

where Γ is the Gamma function, K is the Obukhov-Corrsin constant and $D(\rho, T)$ is the thermal diffusivity of air (Andreas, 1992).

When $\zeta < 0$ we are in an unstable atmospheric surface layer. In the unstable case we have

$$\frac{C_T^2 z_{eff}^{2/3}}{T_\star^2} = \frac{a}{(1 - b\zeta)^{2/3}} \rightarrow \pm T_\star = \sqrt{\frac{C_T^2}{a}} z_{eff}^{1/3} (1 - b\zeta)^{1/3}, \quad (7)$$

$$z_{eff} = \frac{z_{eff}}{2b\zeta} \left(1 - \sqrt{1 - \frac{4b\zeta}{z_{eff}} \left[\int_0^1 z(u)^{-2/3} \left(1 - b\zeta \frac{z(u)}{z_{eff}} \right)^{-2/3} G(u) du \right]^{-3/2}} \right), \quad (8)$$

$$u_\star^3 = \frac{\kappa z_{eff} \epsilon}{(1 + d(-\zeta)^{2/3})^{3/2}} \rightarrow u_\star^2 = \frac{\kappa^{2/3} z_{eff}^{2/3} \epsilon^{2/3}}{(1 + d(-\zeta)^{2/3})}, \quad (9)$$

where b and d are empirical constants, and z_{eff} is the effective beam height assuming that the C_T^2 profile satisfies equation 7 for any z along $z(u)$ (Hartogensis et al., 2003).

Error is propagated from the source measurements to the derived variable H_S via the error propagation equation

$$\sigma_f = \sum_{i=1}^N \left(\frac{\partial f}{\partial x_i} \right) \sigma_{x_{s_i}} + \sqrt{\sum_{i=1}^N \left(\frac{\partial f}{\partial x_i} \right)^2 \sigma_{x_{r_i}}^2} + \sigma_{f_c}, \quad (10)$$

where the general derived variable f is a function of general source measurement variables x_1, x_2, \dots, x_N with respective systematic error $\sigma_{x_{s_1}}, \sigma_{x_{s_2}}, \dots, \sigma_{x_{s_N}}$ and with respective independent Gaussian distributed uncertainties with standard deviations $\sigma_{x_{r_1}}, \sigma_{x_{r_2}}, \dots, \sigma_{x_{r_N}}$ as seen in Taylor (1997). Computational error is given by σ_{f_c} . The first and last terms represent an offset from the true solution, whereas the central term is a measure of the width of the error bars.

Error propagation can be studied with Monte-Carlo methods as in Moroni et al. (1990), however this is best reserved for cases where a closed-form error propagation equation cannot be derived. We will seek

a closed-form equation. As a start, it is practical for the purpose of a sensitivity study to rewrite Eq. 10 as

$$\frac{\sigma_f}{f} = \sum_{i=1}^N S_{f,x_i} \frac{\sigma_{x_{s_i}}}{x_{s_i}} + \sqrt{\sum_{i=1}^N S_{f,x_i}^2 \frac{\sigma_{x_{r_i}}^2}{x_{r_i}^2}} + \frac{\sigma_{f_c}}{f}, \quad (11)$$

where $S_{f,x}$ are unitless sensitivity functions defined by

$$S_{f,x} \equiv \frac{x}{f} \left(\frac{\partial f}{\partial x} \right). \quad (12)$$

The sensitivity functions are each a measure of the portion of the error in the derived variable f resulting from error on each individual source measurement x (Andreas, 1992). Our goal is to evaluate $S_{H_S,z}(u)$, where the height profile $z(u)$ is distributed, hence functional derivatives will be used as in Gruber et al. (2014). We have

$$S_{H_S,z}(u) = \frac{z(u)}{H_S} \left(\frac{\delta H_S}{\delta z}(u) \right). \quad (13)$$

The sensitivity function $S_{H_S,z}$ for this measurement strategy over flat terrain has been evaluated in Gruber and Fochesatto (2013).

We will solve for the sensitivity function in equation 13 for stable conditions in section 2. In section 3 we will solve for the sensitivity function in equation 13 for unstable conditions. In section 4 we will apply the sensitivity function to the topography of a real field site. We conclude in section 5.

2. Stable case ($\zeta > 0$)

Here we can combine equations 2, 3 and 5 to arrive at

$$\zeta^2 + c\zeta^{8/3} = \hat{A}(1 + h\zeta^{3/5})^2 z_{eff}^{4/3}, \quad (14)$$

where

$$\hat{A} \equiv \frac{\kappa^{2/3} g^2 C_T^2}{T^2 a \epsilon^{4/3}}. \quad (15)$$

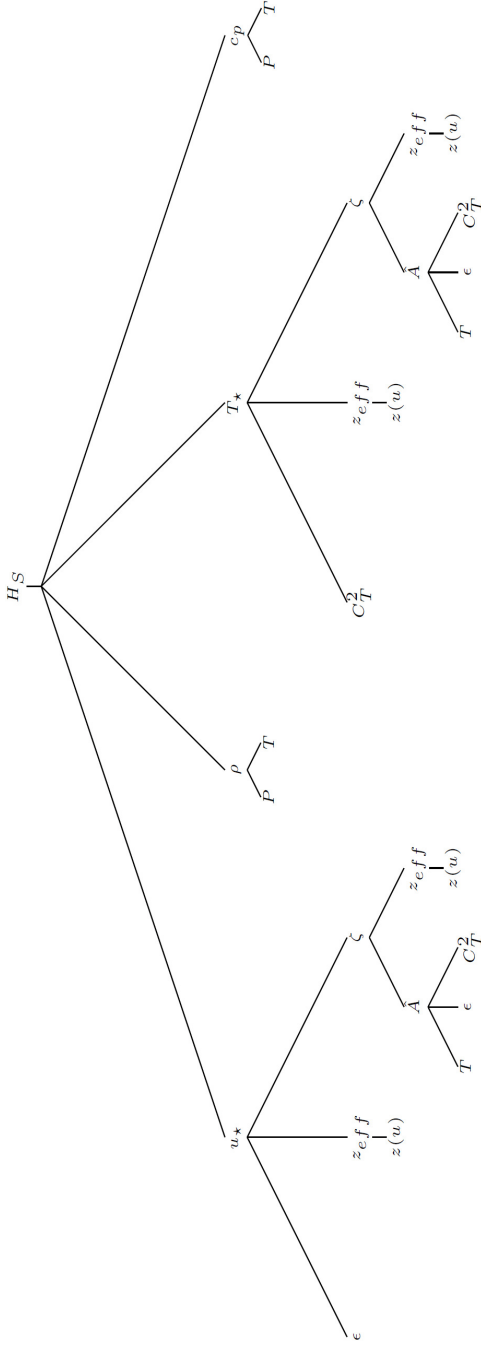


Figure 1. Variable inter-dependency tree diagram for H_S under stable conditions corresponding to $\zeta > 0$. The tree diagram for the dependence of ϵ on P , T and l_o is omitted.

Since z_{eff} is determined independently from equation 4, equation 14 is a single equation in the single unknown ζ , where all other variables in the equation are measured. From this equation we can determine the variable inter-dependency as illustrated in the tree diagram seen in figure 1.

From the tree diagram seen in figure 1, we have

$$\left(\frac{\delta H_S}{\delta z}(u)\right) = \frac{\partial H_S}{\partial T_*} \left[\left(\frac{\partial T_*}{\partial z_{eff}}\right) + \left(\frac{\partial T_*}{\partial \zeta}\right) \left(\frac{\partial \zeta}{\partial z_{eff}}\right) \right] \left(\frac{\delta z_{eff}}{\delta z}(u)\right) + \frac{\partial H_S}{\partial u_*} \left[\left(\frac{\partial u_*}{\partial z_{eff}}\right) + \left(\frac{\partial u_*}{\partial \zeta}\right) \left(\frac{\partial \zeta}{\partial z_{eff}}\right) \right] \left(\frac{\delta z_{eff}}{\delta z}(u)\right). \quad (16)$$

Many of these derivatives follow directly from the definitions. For $\left(\frac{\partial \zeta}{\partial z_{eff}}\right)$ we must implicitly differentiate both sides of equation 14 to arrive at

$$\left(\frac{\partial \zeta}{\partial z_{eff}}\right) = \frac{4(\zeta^2 + c\zeta^{8/3})}{3z_{eff} \left(2\zeta + \frac{8}{3}c\zeta^{5/3} - \frac{6}{5}h \left(\frac{\zeta^{8/5} - c\zeta^{34/15}}{1+h\zeta^{3/5}}\right)\right)}. \quad (17)$$

We then achieve

$$\frac{z(u)}{H_S} \left(\frac{\delta H_S}{\delta z}(u)\right) = \left[\frac{2}{3} - \left(\frac{c\zeta^{2/3}}{3(1+c\zeta^{2/3})} + \frac{3h\zeta^{3/5}}{10(1+h\zeta^{3/5})}\right) \left(\frac{\frac{4}{3}(1+c\zeta^{2/3})}{2 + \frac{8}{3}c\zeta^{2/3} - \frac{6}{5}h \left(\frac{\zeta^{3/5} - c\zeta^{19/15}}{1+h\zeta^{3/5}}\right)}\right) \right] \frac{z(u)^{-2/3}G(u)}{\int_0^1 z(u)^{-2/3}G(u)du}. \quad (18)$$

3. Unstable case ($\zeta < 0$)

Here we combine equations 2, 7 and 9; we achieve

$$\frac{\zeta}{z_{eff}} = -\check{A}\Phi(\zeta), \quad (19)$$

where

$$\check{A} = \frac{\sqrt{\kappa}g^{3/2}(C_T^2)^{3/4}}{T^{3/2}\epsilon a^{3/4}}, \quad (20)$$

$$\Phi(\zeta) = \sqrt{\frac{(1 - b\zeta)(1 + d(-\zeta)^{2/3})^3}{(-\zeta)}}. \quad (21)$$

In the unstable case, z_{eff} is coupled to ζ through equation 8. We input equation 19 into equation 8 to arrive at

$$\zeta = \frac{1}{2b} \left(1 - \sqrt{1 + 4b\check{A}\Phi(\zeta) \left[\int_0^1 (z(u) + bz(u)^2\check{A}\Phi(\zeta))^{-2/3} G(u)du \right]^{-3/2}} \right). \quad (22)$$

This is a single equation in the single unknown ζ , where all other variables are measured. This equation is in fixed point form and can be solved numerically via fixed point recursion as seen in Traub (1964) and in Agarwal et al. (2001). The variable interdependency is mapped out in the tree diagram seen in figure 2.

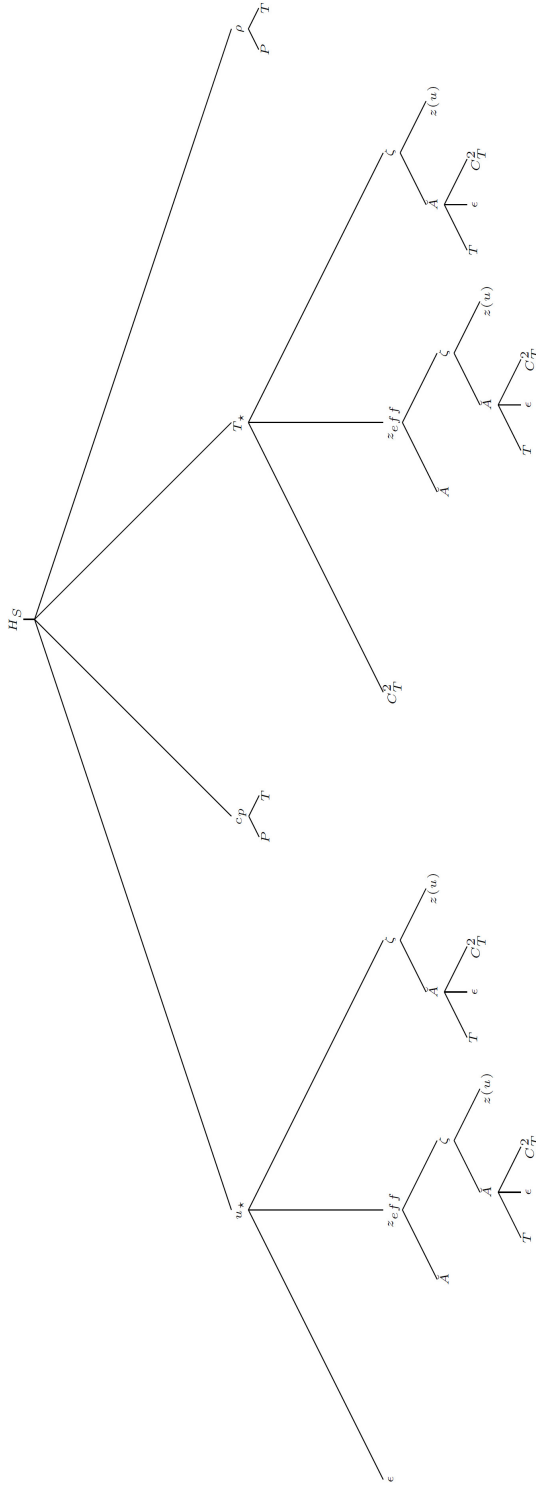


Figure 2. Variable inter-dependency tree diagram for H_S under unstable conditions corresponding to $\zeta < 0$. The tree diagram for the dependence of ϵ on P , T and l_o is omitted.

From the tree diagram seen in figure 2 we have

$$\left(\frac{\delta H_S}{\delta z}(u)\right) = \frac{\partial H_S}{\partial T_*} \left[\left(\frac{\partial T_*}{\partial \zeta}\right) \left(\frac{\partial z_{eff}}{\partial \zeta}\right) \right] \left(\frac{\delta \zeta}{\delta z}(u)\right) + \left(\frac{\partial T_*}{\partial z_{eff}}\right) \left(\frac{\partial z_{eff}}{\partial \zeta}\right) \left(\frac{\delta \zeta}{\delta z}(u)\right) + \frac{\partial H_S}{\partial u_*} \left[\left(\frac{\partial u_*}{\partial \zeta}\right) \left(\frac{\partial z_{eff}}{\partial \zeta}\right) \right] \left(\frac{\delta \zeta}{\delta z}(u)\right) + \left(\frac{\partial u_*}{\partial z_{eff}}\right) \left(\frac{\partial z_{eff}}{\partial \zeta}\right) \left(\frac{\delta \zeta}{\delta z}(u)\right). \quad (23)$$

From equation 19 we have

$$\frac{\partial z_{eff}}{\partial \zeta} = z_{eff} \left(\frac{1}{\zeta} - \frac{\left(\frac{\partial \Phi}{\partial \zeta}\right)}{\Phi(\zeta)} \right), \quad (24)$$

and from equation 21 we have

$$\left(\frac{\partial \Phi}{\partial \zeta}\right) = \frac{1}{2\Phi(\zeta)} \left[\frac{(1 + d(-\zeta)^{2/3})^3 + 2d\zeta(1 - b\zeta)(1 + d(-\zeta)^{2/3})^2(-\zeta)^{-1/3}}{\zeta^2} \right]. \quad (25)$$

From equation 22 we have

$$\left(\frac{\delta \zeta}{\delta z}(u)\right) = \frac{-\left(\frac{\delta f}{\delta z}(u)\right)_\zeta}{\left(\frac{\partial f}{\partial \zeta}\right) + 4b(1 - 2b\zeta)}, \quad (26)$$

where

$$f\left(\check{A}, z(u), \zeta(\check{A}, z(u))\right) \equiv 1 + 4b\check{A}\Phi(\zeta) \left[\int_0^1 \left(z(u) + b\check{A}\Phi(\zeta)z(u)^2\right)^{-2/3} G(u)du \right]^{-3/2}. \quad (27)$$

We thus have

$$\frac{z(u)}{H_S} \left(\frac{\delta H_S}{\delta z}(u)\right) = z(u) \left[\frac{2}{3} \left(\frac{1}{\zeta} - \frac{\left(\frac{\partial \Phi}{\partial \zeta}\right)}{\Phi(\zeta)}\right) + \frac{d}{3(1 + d(-\zeta)^{2/3})(-\zeta)^{1/3}} - \frac{b}{3(1 - b\zeta)} \right] \left(\frac{\delta \zeta}{\delta z}(u)\right), \quad (28)$$

from equation 23, where $\left(\frac{\delta\zeta}{\delta z}(u)\right)$ is solved through equation 26 as

$$\left(\frac{\delta\zeta}{\delta z}(u)\right) = \frac{-\check{A}\Phi(\zeta) \left(z(u) + b\check{A}\Phi(\zeta)z(u)^2\right)^{-5/3} \left(1 + 2b\check{A}z(u)\Phi(\zeta)\right) G(u)}{\check{A} \left(\frac{\partial\Phi}{\partial\zeta}\right) \left[\int_0^1 \left(z(u) + b\check{A}\Phi(\zeta)z(u)^2\right)^{-2/3} G(u) du\right] + b\check{A}^2\Phi(\zeta) \left(\frac{\partial\Phi}{\partial\zeta}\right) \left[\int_0^1 \left(z(u) + b\check{A}\Phi(\zeta)z(u)^2\right)^{-5/3} z(u)^2 G(u) du\right] + (1 - 2b\zeta) \left[\int_0^1 \left(z(u) + b\check{A}\Phi(\zeta)z(u)^2\right)^{-2/3} G(u) du\right]} \quad (29)$$

4. Results

We have solved the sensitivity function $S_{H_S, z}(u)$ which depends on $z(u)$ and ζ for both stable conditions where $\zeta > 0$ and for unstable conditions where $\zeta < 0$. In order to visualize the sensitivity function, we will demonstrate it with a field site beam path height profile $z(u)$. We use the Innvavit basin field site seen in figure 3.

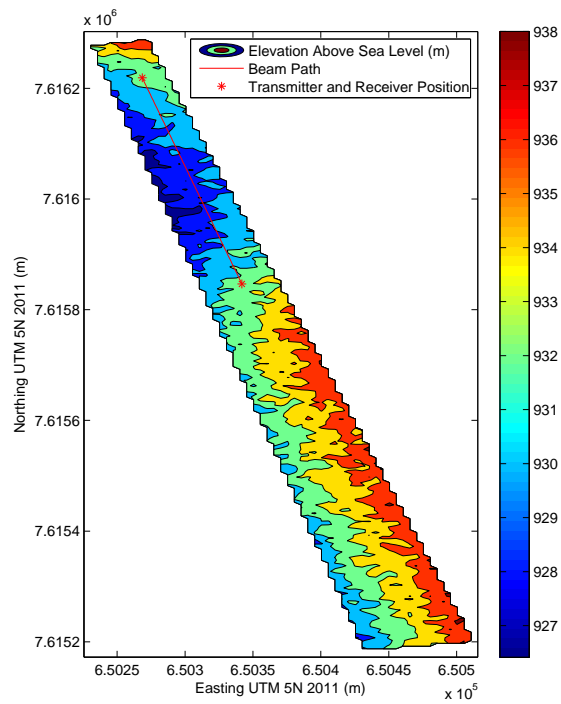


Figure 3. Innavait basin topography and beam path. Innavait basin is located on the North Slope of Alaska. The beam emitter and receiver are raised on tripods 1.8m high.

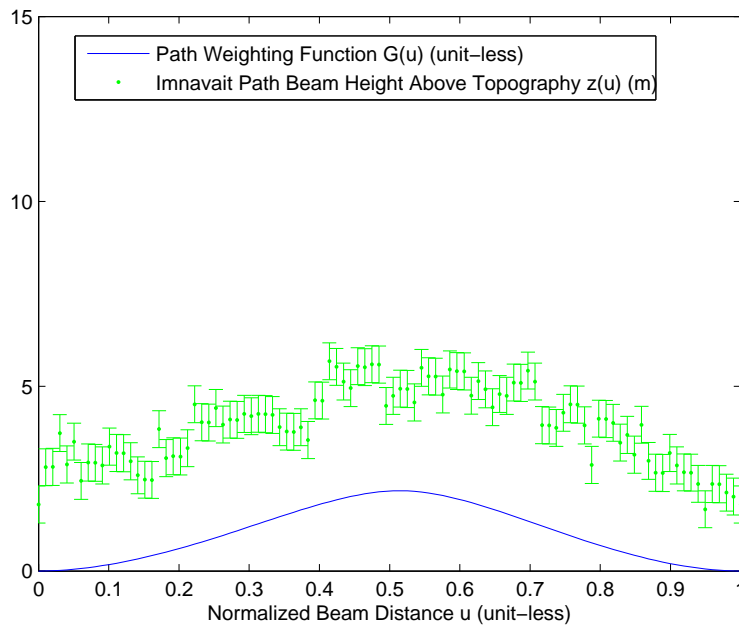


Figure 4. Imnavait basin beam path heights above topography. Imnavait basin is located on the North Slope of Alaska. The beam emitter and receiver are raised on tripods 1.8m high.

This field site has a beam height $z(u)$ as seen in figure 4. A random error component of 0.5m is used in figure 4 since the difference between ground truth GPS measurements and the digital elevation map used has a standard deviation of approximately 0.5m as seen in figure 5. Note that the magnitude of the error does not influence the results of this study.

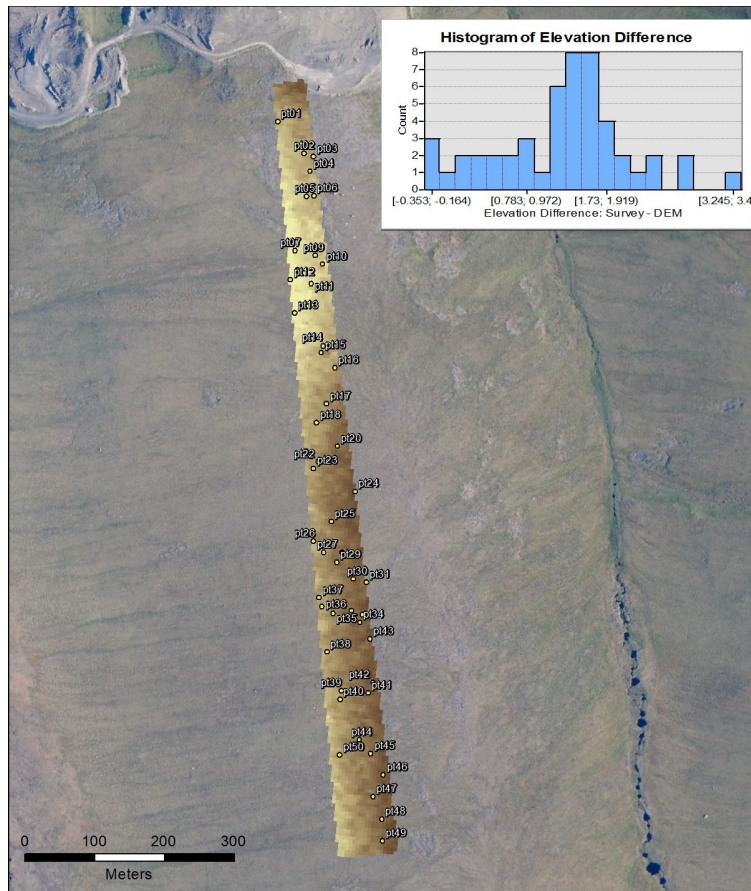


Figure 5. Innavait basin ground truth GPS measurements. Overlaid is a histogram of the difference between the GPS measurements and the digital elevation map used in figures 3 and 4. The standard deviation is approximately $0.5m$.

For the Innavait basin path $z(u)$ seen in figure 4, taking equation 18 for the stable case, and equations 28 and 29 for the unstable case, we arrive at the sensitivity function seen in figure 6. Note that values of \dot{A} for a given ζ in equation 29 follow from the numerical solution to equation 22.

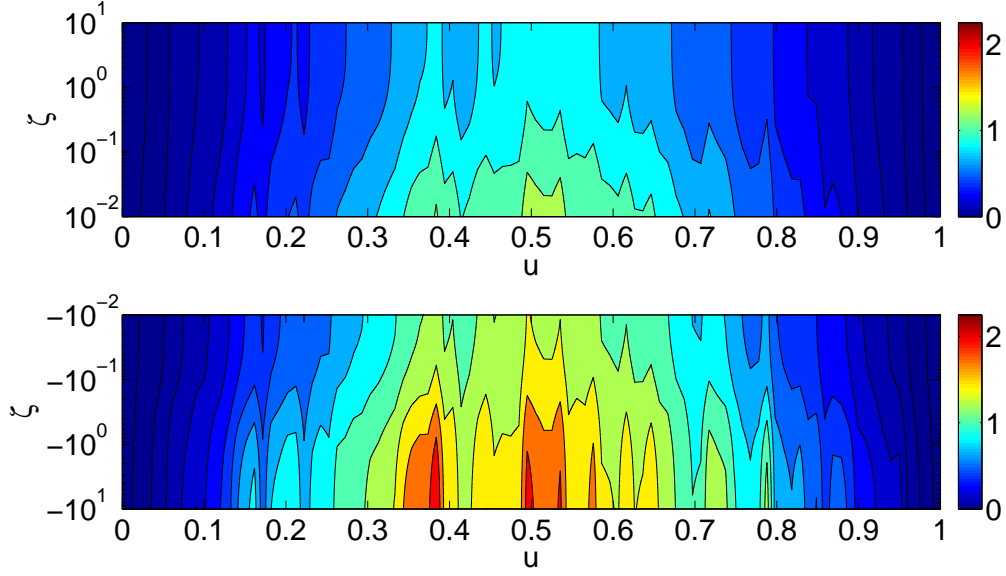


Figure 6. Sensitivity function $S_{H_S, z}(u)$ over the Imnavait basin field site seen in figure 3 and in figure 4.

The sensitivity gets higher from stable conditions to unstable conditions, and it is focused in areas near the center of the beam path, as well as in areas of topographic protrusion. Note the clear spikes in sensitivity at $u = 0.38$ and at $u = 0.5$ in figure 6. These points in the path correspond to local minima in $z(u)$ as seen in figure 4. This makes sense since C_T^2 decreases nonlinearly in height above the ground, most rapidly near the surface. In areas where the beam approaches the ground, the gradient in C_T^2 is higher as seen in equations 3 and 7, therefore uncertainties in the actual height of the beam in those areas will translate into high uncertainties in the derived variables.

Note that if we consider a constant ratio of $\frac{\sigma_z(u)}{z(u)}$, the term in, for example Eq. (11), can be re-written as

$$\int_0^1 \frac{\sigma_z(u)}{z(u)} S_{H_S, z}(u) du = \frac{\sigma_z(u)}{z(u)} \left[\int_0^1 S_{H_S, z}(u) du \right], \quad (30)$$

where the term in square brackets is plotted in figure 7.

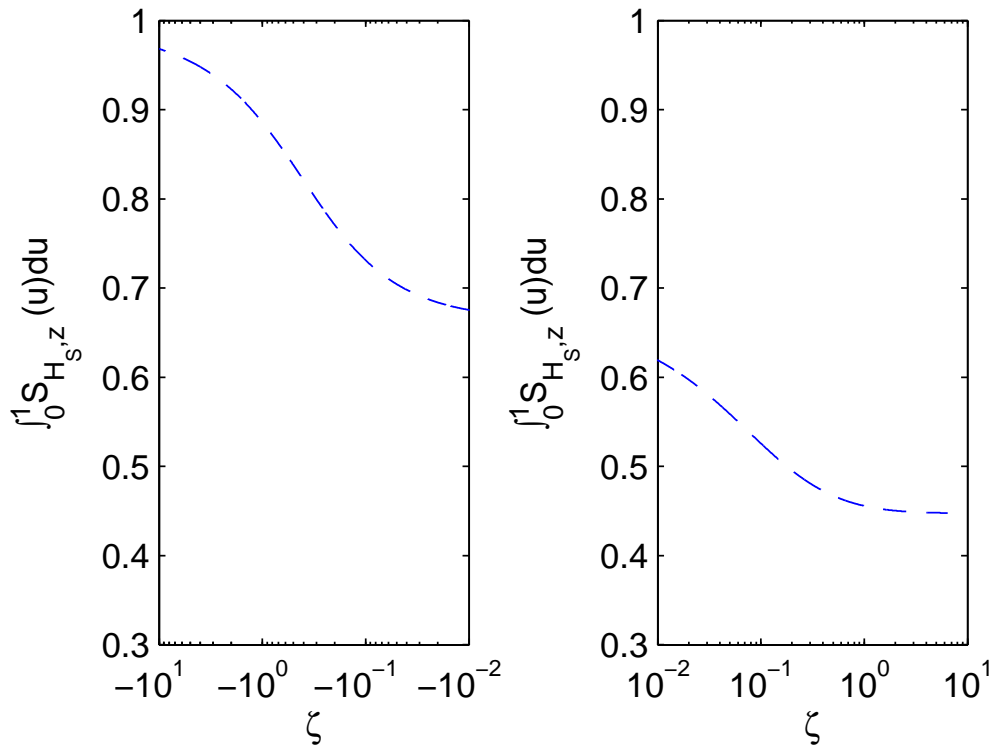


Figure 7. Sensitivity function $S_{H_{S,z}}(u)$ integrated over u for any field site.

This result is the average value of the sensitivity along the whole length of the path, and it converges to the same result for all paths. The sensitivity function in figure 7 is compatible with the one-dimensional sensitivity function for flat terrain seen in Gruber and Fochesatto (2013).

5. Conclusion

Using the effective beam height extension of the Monin-Obukhov similarity equations to variable terrain, we have solved for how uncertainty in topographic heights propagates to displaced-beam scintillometer measurements of turbulent heat fluxes over any field site. We have found that uncertainty is concentrated in areas around topographic protuberances, as well as near the center of the beam path as seen in figures 4 and 6. The local sensitivity can easily approach values of 200% in unstable conditions as seen in figure 6, but the average sensitivity over the beam path never exceeds 100% as seen in figure 7. These

results carry important ramifications in the selection of beam paths, in the calculation of uncertainty, and in the type of topographic data used. It may be that for many scintillometer beam paths, in order to achieve reasonable uncertainty we must use high precision LIDAR topographic data in order to reduce what is likely the greatest contributor to overall uncertainty.

It is interesting that the average value of the sensitivity function $S_{H_S,z}(u)$ over the beam path reduces to the identical sensitivity function $S_{H_S,z}$ for displaced-beam scintillometers over flat terrain as seen in figure 7 and in Gruber and Fochesatto (2013). We have essentially expanded the flat terrain sensitivity function first explored in Andreas (1992) from one dimension to two, and then we averaged through one dimension to arrive back at the original one-dimensional sensitivity function. Future work should perhaps focus on applying this type of sensitivity analysis on large aperture scintillometers using the Businger-Dyer relation to obtain path averaged u_* , T_* and H_S measurements. Additional work should be performed for scintillometer paths which are below the blending height over heterogeneous terrain (Wieringa, 1986; Mason, 1987; Claussen, 1990; Claussen, 1995; Meijninger et al., 2002; Hartogensis et al., 2003; Lu et al., 2009).

Acknowledgements

Matthew Gruber thanks the Geophysical Institute for its support during his Master's degree program in Atmospheric Sciences at the University of Alaska Fairbanks. We thank Jason Stuckey and Randy Fulweber at ToolikGIS, Chad Diesinger at Toolik Research Station, and Matt Nolan at the Institute for Northern Engineering for the digital elevation map of Innavaik, data support, field site GPS measurements and figure 5.

References

- Agarwal RP, Meehan M, O'Regan D (2001) Fixed Point Theory and Applications. Cambridge University Press, Cambridge, 184 pp
- Andreas EL (1989) Two-Wavelength Method of Measuring Path-Averaged Turbulent Surface Heat Fluxes. *J Atmos Oceanic Tech* 6:280–292.
- Andreas EL (1992) Uncertainty in a Path Averaged Measurement of the Friction Velocity u_* . *J Appl Meteorol* 31:1312–1321
- Claussen M (1990) Area-Averaging of Surface Fluxes in a Neutrally Stratified, Horizontally Inhomogeneous Atmospheric Boundary Layer. *Atmos Environ* 24a:1349–1360

- Claussen M (1995) Flux Aggregation at Large Scales: On the Limits of Validity of the Concept of Blending Height. *J Hyrol* 166:371–382
- deBruin HAR, Meijninger WML, Smedman A-S, Magnusson M (2002) Dispaced-Beam Small Aperture Scintillometer Test. Part I: The WINTeX Data-Set. *Boundary-Layer Meteorol* 105:129–148
- Evans J, deBruin HAR (2011) The Effective Height of a Two-Wavelength Scintillometer System. *Boundary-Layer Meteorol* 141:165–177
- Geli HME, Neale CMU, Watts D, Osterberg J, deBruin HAR, Kohsiek W, Pack RT, Hipps LE (2012) Scintillometer-Based Estimates of Sensible Heat Flux Using Lidar-Derived Surface Roughness. *J Hydrometeorol* 13:1317–1331
- Gruber M, Fochesatto GJ (2013) A New Sensitivity Analysis and Solution Method for Scintillometer Measurements of Area-Averaged Turbulent Fluxes. *Boundary-Layer Meteorol*, DOI 10.1007/s10546-013-9835-9
- Gruber M, Fochesatto GJ, Hartogensis OK (2014) Sensitivity of Large-Aperture Scintillometer Measurements of Area-Averaged Heat Fluxes to Uncertainties in Topographic Heights. *Atmos Meas Tech*, 7:33–68, doi:10.5194/amtd-7-33-2014
- Hartogensis OK, deBruin HAR, Van de Wiel BJH (2002) Dispaced-Beam Small Aperture Scintillometer Test. Part II: CASES-99 Stable Boundary-Layer Experiment. *Boundary-Layer Meteorol* 105:149–176
- Hartogensis OK, Watts CJ, Rodriguez J-C, deBruin HAR (2003) Derivation of an Effective Height for Scintillometers: La Poza Experiment in Northwest Mexico. *J Hydrometeorol* 4:915–928
- Hill RJ (1988) Comparison of Scintillation Methods for Measuring the Inner Scale of Turbulence. *Appl Optics* 27(11):2187–2193
- Kleissl J, Gomez J, Hong S-H, Hendrickx JMH, Rahn T, Defoor WL (2008) Large Aperture Scintillometer Intercomparison Study. *Boundary-Layer Meteorol* 128:133–150
- Lu L, Liu S, Xu Z, Yang K, Cai X, Jia L, Wang J (2009) The Characteristics and Parameterization of Aerodynamic Roughness Length over Heterogeneous Surfaces. *Adv Atm Sci* 26:180–190
- Mason PF (1987) The Formation of Areal-averaged Roughness Lengths. *Quart J Roy Met Soc* 114:339–420
- Meijninger WML, Hartogensis OK, Kohsiek W, Hoedjes JCB, Zuurbier RM, deBruin HAR (2002) Determination of Area-Averaged Sensible Heat Fluxes With A Large Aperture Scintillometer Over a Heterogeneous Surface - Flevoland Field Experiment. *Boundary-Layer Meteorol* 105:37–62
- Moroni C, Navarra A, Guzzi R (1990) Estimation of the Turbulent Fluxes in the Surface Layer Using the Inertial Dissipative Method: a Monte Carlo Error Analysis. *Appl Optics* 6:2187–2193
- Solignac PA, Brut A, Selves J-L, Bétéille J-P, Gastellu-Etchegorry J-P, Keravec P, Béziat P, Ceschia E (2009) Uncertainty Analysis of Computational Methods for Deriving Sensible Heat Flux Values from Scintillometer Measurements. *Atmos Meas Tech* 2:741–753
- Sorbjan Z (1989) *Structure of the Atmospheric Boundary Layer*. Prentice-Hall, Englewood Cliffs, New Jersey, 317 pp
- Taylor J (1997) *An Introduction to Error Analysis: The Study of Uncertainties in Physical Measurements*, 2nd edition. University Science Books, Sausalito, California, 327 pp
- Traub JF (1964) *Iterative Methods for the Solution of Equations*. Prentice-Hall, Englewood Cliffs, New Jersey, 310 pp

- Wieringa J (1986) Roughness-Dependent Geographical Interpolation of Surface Wind Speed Averages. *Quart J Roy Met Soc* 112:867–889
- Wyngaard JC, Izumi Y, Collins Jr. SA (1971) Behavior of the Refractive Index Structure Parameter Near the Ground. *J Opt Soc Amer* 61:1646–1650
- Wyngaard JC, Côté OR (1971) The Budgets of Turbulent Kinetic Energy and Temperature Variance in the Atmospheric Surface Layer. *J Atmos Sci* 28:190–201
- Address for Offprints:* 450 Cote Saint Antoine Road, Westmount, Quebec, Canada, H3Y2J9